Available online at www.sciencedirect.com
ScienceDirect
Journal of the European Ceramic Society 30 (2010) 2365–2374
www.elsevier.com/locate/jeurceramsoc

In situ microscopy observation of liquid flow, zirconia growth, and CO bubble formation during high temperature oxidation of zirconium diboride–silicon carbide

Sindhura Gangireddy [a], Sigrun N. Karlsdottir [b], S.J. Norton [a], J.C. Tucker [a], John W. Halloran [a,*]

[a] *Department of Materials Science and Engineering, University of Michigan, Ann Arbor, MI 48109, USA*
[b] *Department of Materials, Biotechnology and Energy, Innovation Center Iceland, IS-112 Reykjavik, Iceland*

Available online 20 February 2010

Abstract

The oxidation of ZrB_2–SiC composites at 1450–1650 °C was directly observed with *in situ* optical microscopy. Video frames showed the flow of silicate liquids, the formation of zirconia deposits, and the growth and collapse of gaseous bubbles on the oxide surface. Contrast in the incandescence of *in situ* images is analyzed as spatial variations in hue and intensity and related to differences in emissivity of the oxide scale surface features by comparing these hot images with room temperature images. Above 1450 °C, gaseous bubbles were observed to grow and collapse causing perturbations in the liquid oxide on the surface. The bubbles are associated with the evolution of CO from SiC oxidation and the onset is related to the critical temperature where the partial pressure of CO under the oxide scale exceeds atmospheric pressure.

Keywords: Optical microscopy; Borides; Refractories; Composites; *In situ*

1. Introduction

1.1. Ribbon method

Ultra-high temperature ceramics (UHTCs) have recently gained interest as potential materials for a reusable thermal protection system and other components in hypersonic vehicles.[1,2] Typically oxidation experiments have been conducted inside furnaces where it is not practical to directly observe the material while it undergoes high temperature oxidation. The other technique used in studying the high temperature oxidation behavior, arc-jet testing, simulates reentry environment and can allow viewing of the specimen. However, arc-jet testing is very expensive, not easily accessible and not typically instrumented for *in situ* studies.[3] Consequently, oxidation processes have been inferred from post-test analysis of the oxide scale quenched to room temperature, regardless of the oxidation method.[4,5] On the other hand, this study attempts to directly observe the UHTC specimen during high temperature oxidation using the Ribbon Method.[6] It has been verified that the ribbon method reproduces the complex oxide scales which form during high-temperature testing of UHTC. Owing to the special geometry of ribbon specimens and design of the process, only about ∼100 W of power is required to reach 1500–2000 °C. As a result the heat flux from the sample is also small, enabling an optical microscope to approach the hot ribbon and image the surface at magnifications as high as ∼100×. An added advantage of ribbon method is that the fast heating rate (∼450 °C/min) and free cooling rates (∼700 °C/s)[6] allow for samples to be tested easily in cyclic heating conditions while minimizing the effects of pre-oxidation caused by slower heating methods. The video images taken during oxidation showed gradual microstructural changes in the oxide scale due to liquid oxide flow and sudden changes caused by gas bubbles. *In situ* observations are compared with room temperature observations made after successive heating cycles.

1.2. Liquid convection hypothesis of oxide scale formation on ZrB_2–SiC

Our observations are interpreted based on the dynamic evolution of crystalline and liquid features in the oxide in terms of the convective flow mechanism proposed by Karlsdottir et

* Corresponding author. Tel.: +1 7347631051; fax: +1 734763478.
E-mail address: peterjon@umich.edu (J.W. Halloran).

0955-2219/$ – see front matter © 2010 Elsevier Ltd. All rights reserved.
doi:10.1016/j.jeurceramsoc.2010.01.034

al.[7] When ZrB_2–SiC ultra-high temperature ceramic composites are oxidized at high temperatures, they form a complex oxide scale consisting of zirconia skeleton, covered by amorphous oxides, which act as protection barriers against oxidation.[8,9] An explanation for these features has been given by a mechanism proposed by Karlsdottir et al.,[7,10–12] which involves formation of a crystalline zirconia layer with a liquid oxide solution containing Boria–Silica–Zirconia (BSZ liquid), by the oxidation reaction:

$$ZrB_2 + xSiC + \frac{5+3x}{2}O_2 \Rightarrow y[ZrO_2]_{primary} + \{B_2O_3 + xSiO_2 + (1-y)ZrO_2\}_{liq} + xCO \quad (1)$$

For a 15 vol% SiC composite, the condensed oxide products were estimated using a calculated 1500 °C phase diagram.[13] The predicted composition was one-third crystalline zirconia (molar basis) formed by direct oxidation (primary zirconia) and about two-thirds of the liquid oxide with approximate composition 71 mol% B_2O_3 + 18 mol% SiO_2 + 11 mol% ZrO_2, which is referred to as the BSZ (Boria–Silica–Zirconia) liquid. However, boria is volatile at these temperatures and as it evaporates, the remaining liquid becomes rich in silica.

$$\{B_2O_3 + xSiO_2 + (1-y)ZrO_2\}_{liq} => \{B_2O_3\}_{gas} + (1-y)ZrO_2 + x\{SiO_2\}_{liq} \quad (2)$$

The solubility of zirconia in silica-rich melts is lower[12] than in borosilicates, so crystalline zirconia (secondary zirconia) precipitates from the liquid oxide as B_2O_3 evaporates. This secondary zirconia forms deposits at the surface of the oxide scale. Thus above the primary zirconia layer, the oxide scale consists of deposits of secondary zirconia, some fluid BSZ liquid, and a more viscous silica-rich liquid depleted of zirconia and boron oxide. Much smaller micron-sized zirconia particles, designated "tertiary zirconia" also decorate the surface. These tertiary zirconia particles seem to be carried along with the flowing liquids, serving as markers for the flow patterns. The oxide surface, observed under the *in situ* microscope, showed the formation of secondary zirconia and the flow patterns of the liquid glasses, confirming the liquid convection hypothesis.

2. Experimental procedure

2.1. Material fabrication

The UHTC material, ZrB_2–15 vol% SiC was provided by The Institute of Science and Technology for Ceramics (CNR-ISTEC) in Faenza, Italy. Details of the properties and processing have been presented elsewhere.[14] The fabrication of the self-supporting specimens is performed at University of Michigan involving the cutting of the bulk material with a wire-Electrical Discharge Machine (EDM) into 2.3 mm × 2.0 mm × 25 mm bars and then reducing the bar thickness to 400–500 μm in the center with a mechanical grinder (220 grit – diamond wheel) to make the thin hot zones.[6]

2.2. Oxidation testing with in situ microscopy

The ribbon method[6] is used to heat the samples to the testing temperature. The special specimen geometry for this method is shown in Fig. 1B. Electrical current is supplied through the thick ends, which heats the thin central ribbon to high temperature, while the end sections remain cold. The specimen is held by its thick ends onto the conductive specimen holder, as shown in Fig. 1C, with spring pressure from alligator clips (insulated with thin alumina plates). AC current is supplied through current leads to the conductive specimen holder, controlled by the temperature signal from an optical pyrometer (MI-S140, Mikron Infrared, Santa Clara, CA, USA). Details of the power supply, current and temperature control, and performance characteristics were previously reported.[6] The samples are tested in temperature profiles of static oxidation and cyclic oxidation (in steps of 15 or 30 min), at temperatures ranging from 1450 to 1700 °C.

The *in situ* microscopy was performed using a stereo optical microscope (Nikon SMZ 1000, Nikon Instruments Inc., Melville, NY, USA) that was 15–20 cm above the specimen, shown in Fig. 1A. The exact lens distance varies with the focal length for different magnifications (1–8×). The microscope is fitted with a digital camera (01-GO-03-CLR-10, Q-Imaging, Surrey, Canada), and is connected through a computer to capturing software ("QCapture", Q-Imaging, Surrey, Canada). The program provides an interface to view the sample in live preview as well as to capture still images or video. The incandescent radiation emitted from the hot sample is too bright for good visibility and therefore to reduce the intensity, a reflective neutral density filter of 2% optical density (NT48-531, Tech-Spec, Edmund Optics, Barrington, NJ, USA) is fitted over the microscope lens. This filter attenuates the light from the entire spectral range evenly and has a transmission ratio of 1%. The resulting light allowed viewing of features larger than ~10 μm. A video composed of frames snapped every 10 s, which is the allowed lower limit for QCapture programming, is recorded by the camera. The risk of missing important events occurring between the frames was small due to the relatively slow and gradual growth of the oxide scale features at temperatures below 1650 °C, including bubble formation and associated liquid oxide motion.

2.3. Room temperature microscopy with cyclic heating

In cyclic heating, the specimen is cooled to room temperature almost instantly (700 °C/s) after each cycle and then images are taken using the same stereo optical microscope, with external light focused on the sample, giving reflection contrast. These images taken after subsequent cycles of small time periods represent an interesting study of statistics in the formation and growth of the features. The samples were also observed under metallographic optical microscope which can reach higher magnifications and allows study of the microstructure of the oxide scale surface in more detail. Scanning electron microscopy (Philips XL30, FEI, Oregon, NE, USA) was also performed on the samples, but only after oxidation testing was completed since SEM required metallic conducting layer coating after which the sample can no longer be oxidation tested.

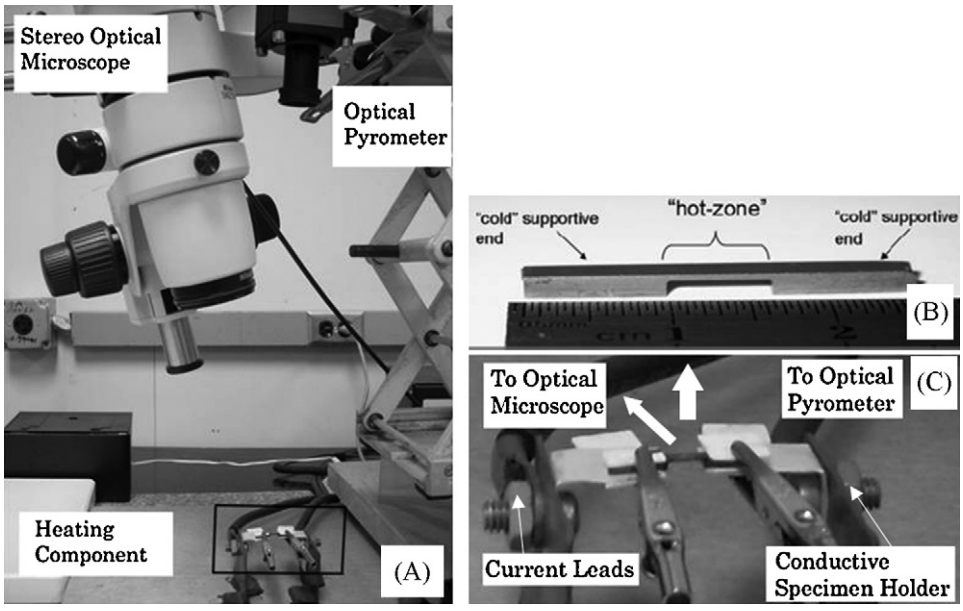

Fig. 1. (A) *In situ* optical microscopy apparatus showing a stereo optical microscope situated over the heating component of the ribbon apparatus (UHTC specimen at room temperature); (B) detail of the UHTC ribbon sample; (C) detail of the heating component of Ribbon method.

3. Results and discussion

3.1. Contrast in incandescence of in situ microscopy

During the high temperature oxidation, *in situ* microscopy uses the incandescent light emitted by the hot specimen, which produces images that are quite different from ordinary optical microscopy images using reflected or transmitted light. The contrast in incandescent light microscopy is recorded as spatial variations in the wavelength (related to hue, *H*) and intensity, *I*, of the incandescent light. This information can be derived from the Red–Green–Blue (RGB) data in each pixel recorded by the camera, and can be quantitatively analyzed to extract hue and intensity.[15] Hue (or color) is related to the wavelength of the emitted light which in turn varies with temperature of the source. Intensity, which is the amount of light in the radiation, is proportional to $\varepsilon_L \times T_L{}^4$ (emissivity and local temperature raised to the fourth power). So hue and intensity are related to the spatial variations in local emissivity (ε_L) and local temperature (T_L) where all hue variations correspond to variations in T_L, and intensity variations – given constant hue, correspond to variations in ε_L. In other words, if the contrast is due to a difference in local temperature, the light and the dark regions differ in both intensity and hue values. On the other hand, if the contrast is due to a difference in local emissivity, intensity will change while hue will remain constant across these regions. Hue and intensity values of dark and light regions in the *in situ* images were compared over several locations of each *in situ* image and further over several images for verification. This comparison showed a shift in intensity while hue remained constant. So the contrast is concluded to arise from the difference in local emissivities of the dark and light regions.

The surface of the oxide scale usually consists of crystalline zirconia and a silica-rich borosilicate liquid. The difference in the typical emissivities of these materials supports the above analysis. The emissivity of crystalline zirconia ranges from 0.62 to 0.75[16] whereas amorphous silica has emissivity ranging from 0.80 to 0.88.[17] This suggests that the regions in brighter contrast must be silica-rich liquid and the features in darker contrast, crystalline zirconia. The areas selected for the analysis are all in the hot zone and are less than 50 μm apart. So temperature differences within such small distances in hot zone should be negligibly small[3] and would not have contributed for the contrast.

3.2. In situ image – comparison with room temperature images

Fig. 2A is an *in situ* image of the oxide scale surface on ZrB_2–15% SiC at 1550 °C after a total of 105 min of cyclic oxidation (15 min steps). The image shows the oxide surface imaged with its incandescent illumination. Fig. 2B shows the same field of view after quenching to room temperature, imaged in reflected light. The comparison of the images was used to identify the dark contrast features in the *in situ* image as secondary zirconia "islands" while the regions in lighter gray contrast are interpreted as silicate-rich liquid oxide, confirming the hypothesis made from contrast analysis correct. Curved lines, faintly visible in the incandescent image are interpreted as "flow lines" in the liquid oxide, the visibility of which is aided by small tertiary zirconia crystals entrained in the flowing liquid. The room temperature image shows the liquid oxide, now quenched to a glass, more clearly and with features suggesting that the liquid oxide emerged from near the zirconia islands and flowed across the surface.

Fig. 3 compares two room temperature images taken of the hot zone showing the oxide scale surface on ZrB_2–15% SiC after cyclic oxidation in air at 1550 °C for 60 min. The first is a reflected light optical image and the other is an SEM image. Zirconia is in bright contrast in the SEM image with silicate glass

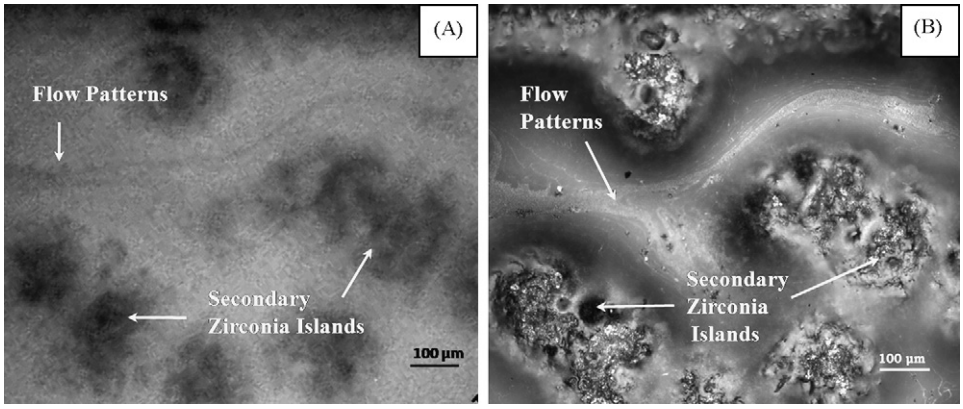

Fig. 2. (A) *In situ* image at 1550 °C after 105 min of oxidation, showing the oxide surface imaged with its incandescent illumination. (B) The same field of view after quenching to room temperature, imaged in reflected light.

in grey contrast. Both images showed clear distinction between turbid glass and clear glass. The liquid areas which are cloudy white in the optical image (and darker grey in the SEM image) have been shown[7] to contain B_2O_3, while the clear glassy areas in the optical image (and lighter grey in the SEM image) are richer in SiO_2. The appearance/location of these glassy regions suggests liquid flow outwards from the zirconia locations, closer to which the glass retained some boria (darker in SEM) whereas the glass farther from the zirconia was richer in SiO_2 (lighter in SEM) owing to boria evaporation. Further evidence of flow comes from the patterns of micron-sized zirconia particles (tertiary zirconia) that decorate the surface, serving as markers for flow.

3.3. Dynamic evolution of oxide scale – in situ images

Fig. 4 shows a series of *in situ* images of the formation and growth of secondary zirconia islands taken during cyclic oxidation at 1550 °C in incandescent illumination. After 1 min of oxidation (Fig. 4A) small secondary zirconia islands appear in dark contrast at locations (a), (b), (c) and (d). After 100 min of oxidation, Fig. 4B shows that these features have grown to about 50 μm across. After 150 min oxidation (Fig. 4C), features (c) and (d) are growing together. Island size data was collected from image frames for several specimens to determine the average diameter of secondary zirconia islands. The size of these features increases gradually with oxidation time up to about 180 min at 1550 °C. Fig. 5 plots the average size as a function of time and shows that the average size increases from 50 ± 10 μm after 15 min to 190 ± 10 μm after 180 min. These values were comparable to previously reported observations of 60 ± 10 μm after 30 min and 115 ± 20 μm at 180 min on quenched samples for conventional furnace oxidation.[11] So until 180 min, the average size increases roughly linearly with time at about 0.8–0.9 μm/min. However, after the next cycle, the boundaries between the islands were less distinct and the average size increased from ~190 to 230 μm, a larger increase than expected from earlier cycles. This is associated with a sudden onset of bubbles forming during oxidation, which are presented in detail in the next section.

3.4. Observation of bubbles

The *in situ* video images taken during oxidation revealed formation and collapse of gas bubbles, called Bubble Burst Events, which had a dramatic effect on the oxide scale features. A bubble burst event, spanning from inception of a bubble until it ruptures, usually took about a minute to complete, owing to the high vis-

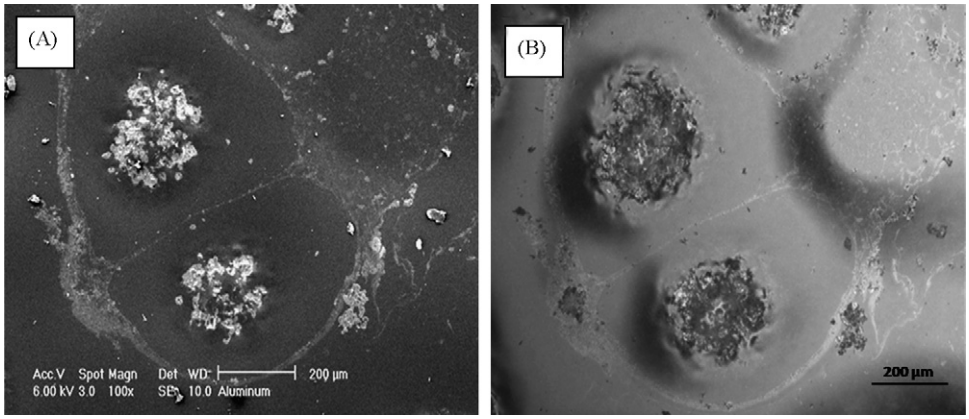

Fig. 3. Features on the surface of ZrB_2–15 SiC after conventional furnace oxidation in air at 1550 °C for 60 min. The same field of view imaged in SEM (left) and optical metallograph using reflected light (right).

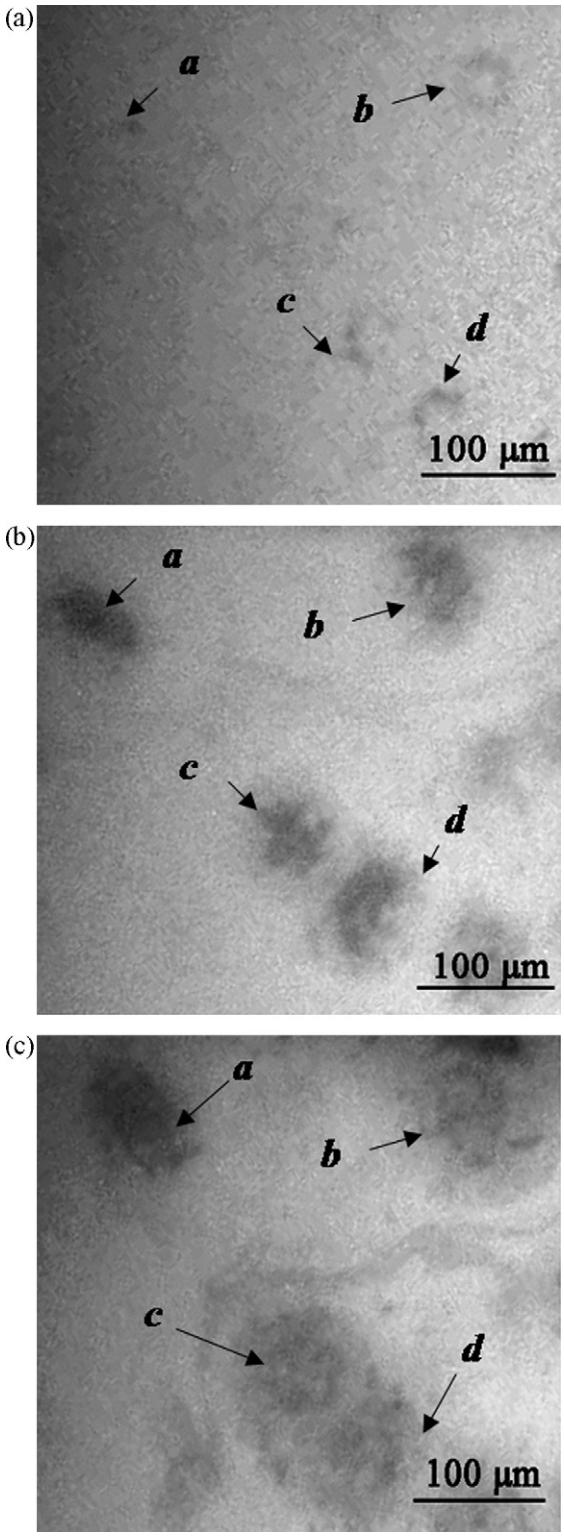

Fig. 4. *In situ* images of the formation and growth of secondary zirconia islands taken during cyclic oxidation at 1550 °C after 1 min of oxidation (A), after 100 min (B), after 150 min (C). The regions of secondary zirconia appear in dark contrast at (a), (b), (c) and (d).

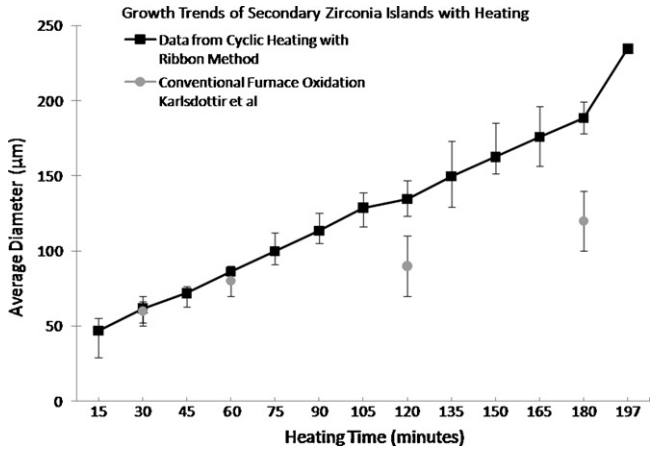

Fig. 5. Diameter of secondary zirconia islands vs. oxidation time at 1550 °C.

cosity of the liquid oxide film. Fig. 6 demonstrates the progress of a large bubble in the hot zone from the time of its formation, at 182 min of heating the specimen at 1550 °C, until it burst one minute later. The sequence of images captures the slow growth of the bubble over the minute, demonstrated by increasing diameter of the bubble marked in dark contrast by the incandescence of *in situ* images. The three dark circles on the right hand side of these images are secondary zirconia. Fig. 6A is taken just before a bubble emerged in the lower left corner of the frame. Fig. 6B is a frame taken 20 s later, and the bubble about 250 µm in diameter is seen in the lower left corner of the image. Fig. 6C is a frame another 40 s, and the bubble has grown to about 400 µm diameter, and impinged upon the two secondary zirconia islands, causing the liquid oxide to flow over the zirconia. The bubble burst and collapsed shortly after this frame. The progress of the bubble boundary is outlined in Fig. 6D, with the position of the zirconia islands also noted.

Fig. 7 shows the same location over the next few minutes of heating illustrating the motion of the liquid oxide caused by the above bubble burst event. This slow sweep of the liquid oxide from the vicinity of the bubble burst event, towards right side of the picture, lasted over 5 min. Fig. 7A is the image taken just after the bubble had burst, at 183 min of heating at 1550 °C. Fig. 7B–D shows the same area 2 min later (185 min), 3 min later (186 min) and 5 min later (187 min) respectively. The shape of the flow pattern, marked (a), which is lined with tertiary zirconia particles in dark contrast, can be compared over this time duration. Fig. 7B shows a definite shift in (a) towards right side, the shift becoming pronounced with progress of time in Fig. 7C and D, as the liquid oxide keeps moving away from bubble burst location, pushing the flow pattern and submerging two secondary zirconia islands in the proximity, marked (b) and (c).

The complete effect of this bubble burst is captured by two room temperature images (optical bright field) taken before, Fig. 7E and after the event, Fig. 7F. The two secondary zirconia islands are in the lower left, features (b) and (c), in Fig. 7E. However in Fig. 7F, (c) is almost covered by glass, and the island is not visible at location (b), as it has been covered by liquid oxide. In bright field, the silica-rich borosilicate glass reflects light off and only the features above the surface are visible. The glass

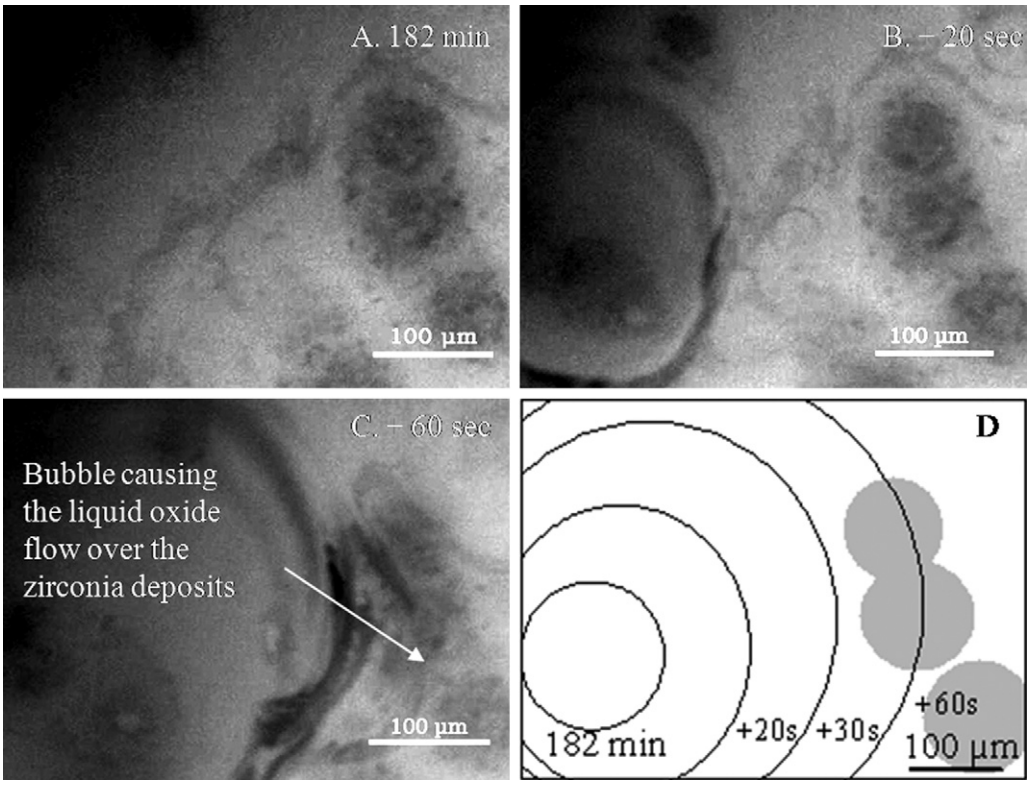

Fig. 6. *In situ* video frames of the formation and collapse of a gas bubble at 1550 °C (A) after 182 min of oxidation; (B) after 182 min and 20 s; (C) after 182 min and 60 s; (D) schematic showing the growth of the bubble with time until it burst and leaving the three zirconia deposits (represented as gray circles) covered with liquid oxide.

that is now covering (b) and (c) has flow patterns with tertiary zirconia particulates, shifted from left due to the bubble burst event. Also, the zirconia island cluster on the right side seems to be larger. Thus bubble formation causes major dynamic changes in the oxide scale microstructure.

3.5. Trends in bubble burst events

The onset temperature and the number of bubbles were observed to depend on the temperature of oxidation. Constant heating is preferred over cyclic heating in studying these trends, owing to the brief spike in temperature by the PID controller while starting a heating profile which could influence the results which are being studied for temperature dependence.

Bubbles were not observed below 1450 °C even after extensive heating over 8 h, but appeared at 1500 °C and above, suggesting an "onset temperature" for bubble formation around 1450–1500 °C. It was also noted that bubbles do not appear immediately, but with a "delay time" requiring certain time of heating that occurs before bubbling is observed. This "delay time" was found to depend on temperature, shown in Fig. 8 (the dashed lines are to demonstrate the trend and are not most fit lines). While below 1450 °C no bubbles formed, above 1650 °C they formed instantly, delay time ~ 0.

The bubbles are usually accompanied with rapid oxidation rates and the sample burns through the thin cross-section of ribbon quite fast, leaving a short period of heating around 15–30 min when bubble bursts are occurring. During this period of time, the number of bubbles observed in the field of view is counted and normalized for "frequency of bubble formation", expressed as the number of bubbles/cm^2 s. In the temperature range where bubbles were observed, the frequency was found to increase steadily with temperature, as shown in Fig. 8. At 1450 °C, where no bubbles were detected the frequency is zero and at 1650 °C, the specimen has quite vigorous bubbling at a rate 16 bubble/cm^2 s where the *in situ* videos showed the surface looking like boiling syrup.

3.6. Thermodynamic analysis of bubble formation

Let us consider the necessary conditions for forming a gas bubble. There must be a source of gas, either generated by a reaction or dissolved in a condensed fluid. To accumulate the gas, the rate of generation of the gas species must be larger than the rate it permeates out. The partial pressure of the species must be sufficient for a bubble to expand against the pressure of the atmosphere, so the pressure inside the bubble must be greater than P_{atm} the external pressure (1 atm in this case). The possible gas species are CO, CO_2, SiO (from SiC) or a boron oxide gas (from ZrB_2). Fahrenholtz estimated the vapor pressures of all boron oxide species to be much smaller than 1 atm at 1527 °C.[18] At the oxygen activity expected near ZrB_2/ZrO_2 oxidation front at 1527 °C ($P_{O_2} \sim 10^{-16}$),[18] the pressure of P_{CO_2} will be much less than P_{CO}. At the same oxygen activity and temperature,

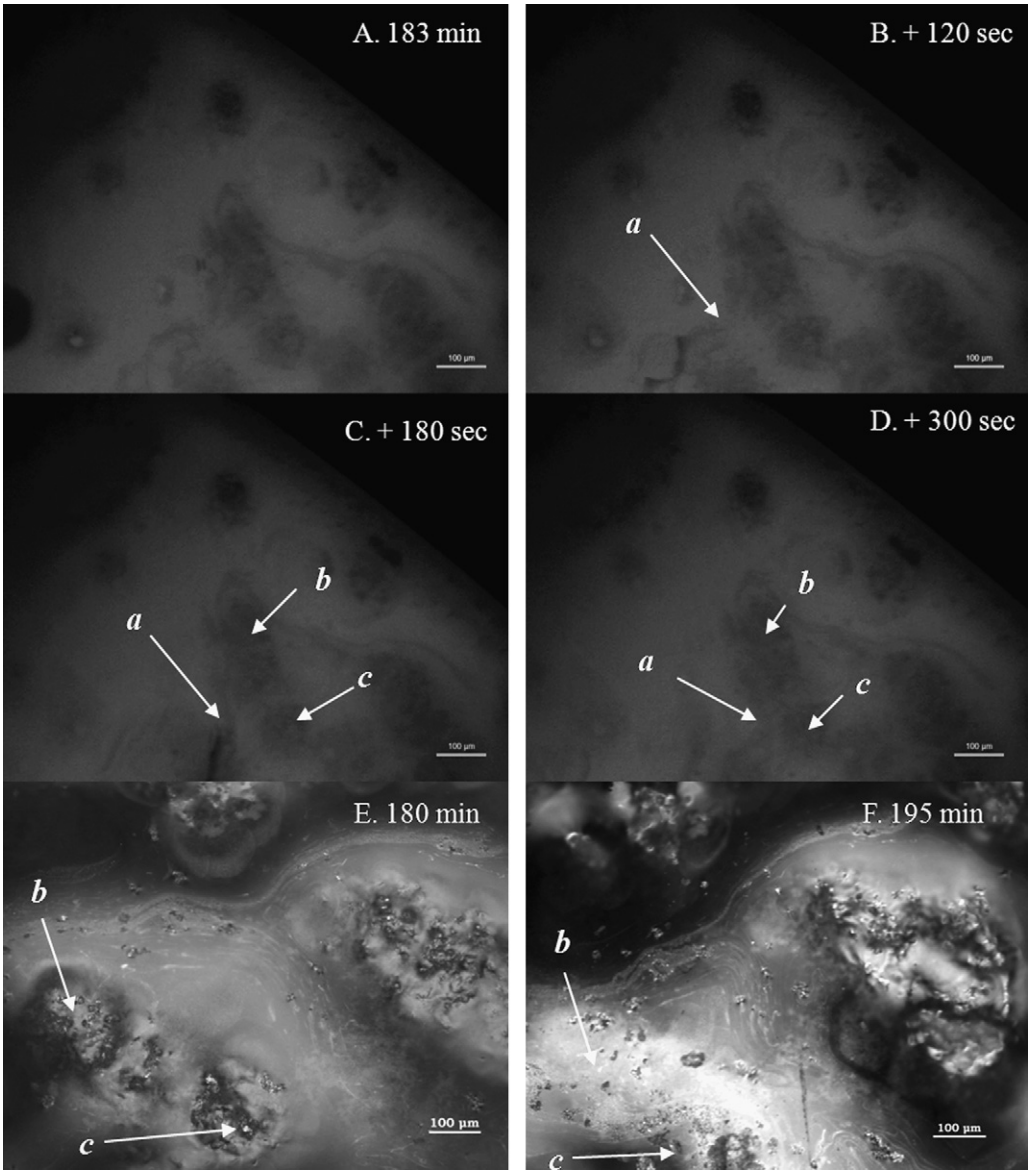

Fig. 7. A–D are *in situ* images taken during oxidation at 1550 °C showing the oxide scale surface over the next 5 min after the bubble burst depicted in Fig. 6, illustrating the motion of the liquid oxide away from the burst location. E and F are bright field optical images taken at room temperature before and after the bubble burst events.

PSiO had been estimated to be <1 atm.[19] Hence we suggest the gas bubbles are most likely composed of CO gas from the oxidation of silicon carbide.

As SiC in the composite oxidizes to CO, one mole of CO is produced for every mole of SiC consumed. This CO can either be in the gas phase and be released as a bubble, or be dissolved in the condensed phases such as the BSZ liquid and permeate to the exterior by diffusion. Permeation of dissolved CO must be the common behavior, since bubbles are not typically observed.[2,20] This may be because oxygen and CO might have similar permeabilities in oxide scales, owing to similar molecular diameters,[21] and the oxidation of ZrB_2–15% SiC requires the ingress of 2.725 mol of O_2 but the egress of only 0.15 mol of CO.

However, under certain conditions, the CO forms gas bubbles. Assuming that the activity of oxygen is same for both the oxidation reactions, those of ZrB_2 and SiC, we can estimate the partial pressure of CO in the bubble, P_{CO}, by considering the equilibrium of ZrB_2 with ZrO_2 and B_2O_3:

$$ZrB_2\,(s) + (5/2)O_2\,(g) = ZrO_2\,(s) + B_2O_3\,(l) \quad (3)$$

With the equilibrium constant is given by

$$K_{ZrB_2} = \frac{a_{ZrO_2} a_{B_2O_3}}{a_{ZrB_2} P_{O_2}^{5/2}} = \exp\left[\frac{-\Delta G^{\circ}_{fB_2O_3} - \Delta G^{\circ}_{fZrO_2} + \Delta G^{\circ}_{fZrB_2}}{RT}\right] \quad (4)$$

in terms of the activities of the components, and the free energies of formation. If we consider passive oxidation of the SiC, the

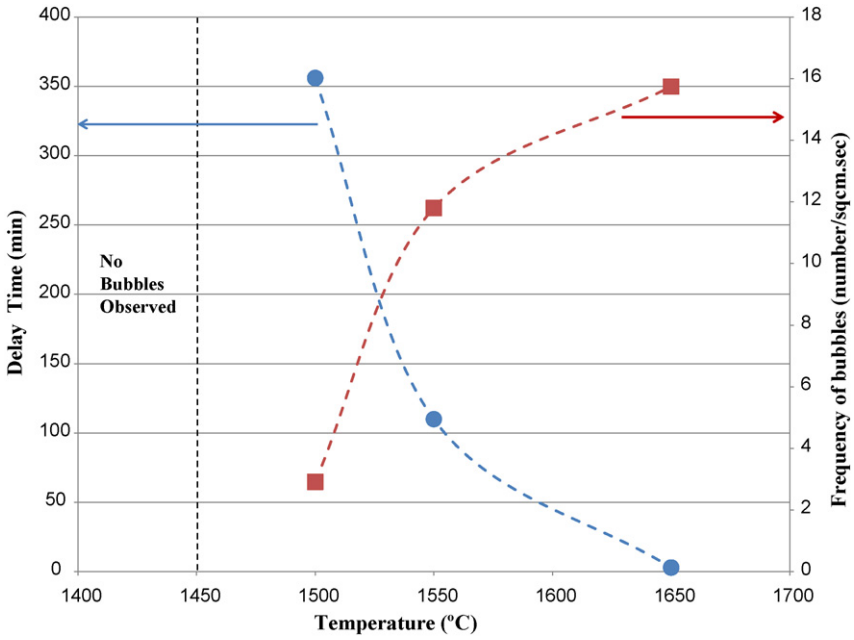

Fig. 8. The delay time before bubbles start to appear and the frequency of bubbles after the delay, while heating at different temperatures in static oxidation profile.

reaction is:

$$\mathrm{SiC\,(s)} + (3/2)\mathrm{O_2\,(g)} = \mathrm{SiO_2\,(l)} + \mathrm{CO\,(g)} \quad (5)$$

With the equilibrium constant is given by

$$K_{\mathrm{SiC}} = \frac{a_{\mathrm{SiO_2}} P_{\mathrm{CO}}}{a_{\mathrm{SiC}} P_{\mathrm{O_2}}^{3/2}} = \exp\left[\frac{-\Delta G^{\circ}_{f\mathrm{SiO_2}} - \Delta G^{\circ}_{f\mathrm{CO}} + \Delta G^{\circ}_{f\mathrm{SiC}}}{RT}\right] \quad (6)$$

which involves both the oxygen activity and the CO partial pressure. If both the silicon carbide and the zirconium diboride are oxidized at the same oxygen activity, we can replace the oxygen partial pressure term in (6) with expression from (4) to obtain an expression of the CO partial pressure under conditions where both equilibrium (3) and (5) obtain:

$$P_{\mathrm{CO}} = \left(\frac{a_{\mathrm{ZrO_2}} a_{\mathrm{B_2O_3}}}{a_{\mathrm{ZrB_2}}}\right)^{3/5} (a_{\mathrm{SiO_2}})^{-1} \frac{K_{\mathrm{SiC}}}{(K_{\mathrm{ZrB_2}})^{3/5}} \quad (7)$$

If we assume that the activity terms for the condensed species in (5) are all ~1, the P_{CO} can be estimated simply from the

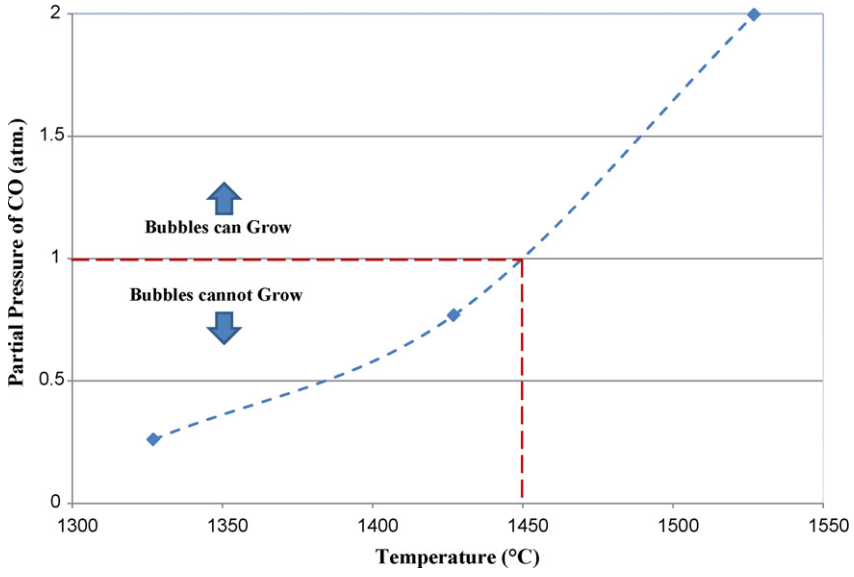

Fig. 9. Partial pressure of CO gas species, formed from passive oxidation of SiC, at the oxidation location as a function of temperature.

standard free energies of formation:

$$P_{CO} = \frac{K_{SiC}}{(K_{ZrB_2})^{3/5}} = \exp\left[\frac{\Delta G^{\circ}_{fSiC} - \Delta G^{\circ}_{fSiO_2} - \Delta G^{\circ}_{fCO} + (3/5)\Delta G^{\circ}_{fB_2O_3} + (3/5)\Delta G^{\circ}_{fZrO_2} - (3/5)\Delta G^{\circ}_{fZrB_2}}{RT}\right] \quad (8)$$

The P_{CO} thus calculated using data from the JANAF thermochemical tables[22] is displayed in Fig. 9. Below 1450 °C, the P_{CO} is lower than the ambient pressure of 1 atm, but above 1450 °C the P_{CO} exceeds the minimum criterion for bubble to be stable. This transition temperature of 1450 °C corresponds well with the experimentally observed "onset temperature" for bubble formation. Thus the thermodynamic analysis gives a justification for a temperature where bubbles begin, but does not seem to explain the time dependence or the "delay time" of Fig. 8.

3.7. Bubble burst events – cause or result?

It is not clear if CO bubbles increase the oxidation rate, or if they are a consequence of faster oxidation, but the bubbles seem to interrupt the slow growth process that dominates the first part of the oxidation and are associated with more rapid growth of the surface features, suggesting faster oxidation. One explanation could be that due to the large size of these bubbles, they can redistribute the liquid oxide and disrupt the protective oxide layer, leading to faster oxidation. Some of the samples show evidence of extensive bubbling and resulting retreat of the liquid oxide with exposed un-reacted material underneath. On the other hand, some other phenomenon might be causing an increase in oxidation rate, which implies increased rate of CO generation beyond the rate which can be removed by permeation and hence causing the bubbles.

Nevertheless, the question remains why CO bubbles have not been described before. One possibility is that they are an artifact of the Ribbon Method. Unlike conventional furnace tests the Ribbon Method uses a specimen of limited thickness. It could be a phenomenon that occurs only in nearly fully oxidized ribbons. This method also uses direct resistive heating, where the interior of the sample is hotter than the surface, which could possibly cause bubbles that do not form in isothermal samples. However, it is also possible that the bubbles simply have not been noticed, or have not caught the interest of previous researchers. Perhaps the hot bulk ZrB_2–SiC specimens have bubbles during conventional furnace oxidation, but the ~1 min lifetime of bubbles is so brief that they collapse and disappear during cooling from furnace oxidation temperature.

4. Conclusion

Direct observations of high temperature oxidation behavior of ZrB_2–SiC UHTC were achieved using *in situ* microscopy through a simple apparatus. Local variation in the incandescent light emitted from the hot sample provided the contrast in the images from the *in situ* optical microscopy. This contrast was analyzed to discover the origin to from the differences in the emissivity of crystalline zirconium dioxide and liquid silicon dioxide. *In situ* videos captured the evolution of the oxide scale ZrB_2–SiC ultra-high temperature ceramics undergoing oxidation, and showed the gradual growth zirconia regions and the flow of liquid silicate oxide, thus providing evidence of dynamic evolution of crystalline and liquid features in the oxide in terms of fluid flow mechanisms.

The formation, growth, and collapse of bubbles during the oxidation of ZrB_2–15% SiC were at 1450–1650 °C were observed. No bubbles were reported below an onset temperature of 1450 °C. Above this temperature, bubbles were not observed until after a delay time, an extended period of oxidation. The delay time decreased at higher temperatures and the frequency of bubble formation was found to increase with temperature of oxidation. Thermodynamic calculation of the carbon monoxide partial pressure presumed to exist at the boride + carbide/oxide interface showed that the CO pressure should exceed one atmosphere at around 1450 °C, which is close to the experimentally observed onset temperature. Overall, the emergence, growth, and collapse of the bubbles cause significant motion of the liquid oxide, and drastic changes in the scale microstructure.

Acknowledgement

We thank the Office of Naval Research for funding this research under grant N00014-02-1-0034.

References

1. Zimmermann JW, Hilmas GE, Fahrenholtz WG, Monteverde F, Bellosi A. Fabrication and properties of reactively hot pressed ZrB_2–SiC ceramics. *J Eur Ceram Soc* 2007;**27**(7):2729–36.
2. Rezaie A, Fahrenholtz WG, Hilmas GE. Evolution of structure during the oxidation of zirconium diboride–silicon carbide in air up to 1500 °C. *J Eur Ceram Soc* 2007;**27**(6):2495–501.
3. Karlsdottir SN. Oxidation behavior of zirconium diboride–silicon carbide composites at high temperatures. PhD thesis. Ann Arbor, MI: University of Michigan; 2007.
4. Gasch M, Ellerby D, Irby E, Beckman S, Gusman M, Johnson S. Processing, properties and arc jet oxidation of hafnium diboride/silicon carbide ultra high temperature ceramics. *J Mater Sci* 2004;**19**:5925–37.
5. Chamberlain A, Fahrenholtz W, Hilmas G, Ellerby D. Oxidation of ZrB_2–SiC ceramics under atmospheric and reentry conditions. *Refrac Appl Trans* 2005;**1**(2):1–8.
6. Karlsdottir SN, Halloran JW. Rapid characterization of ultra-high temperature ceramics. *J Am Ceram Soc* 2007;**90**(10):3233–8.
7. Karlsdottir SN, Halloran JW, Henderson CE. Convection patterns in liquid oxide films on ZrB_2–SiC composites oxidized at high temperature. *J Am Ceram Soc* 2007;**90**(9):2863–7.
8. Monteverde F, Bellosi A. The Resistance to oxidation of HfB_2–SiC composite. *J Eur Ceram Soc* 2005;**7**:1025–31.
9. Talmy IG, Zaykoski JA, Opeka MM. Properties of ceramics in the ZrB_2/ZrC/SiC system prepared by reactive processing. *Ceram Eng Sci Pro* 1998;**19**(3):105–12.
10. Karlsdottir SN, Halloran JW. Formation of oxide films on zirconium diboride–silicon carbide composites during oxidation: evolution with time and temperature. *J Am Ceram Soc* 2009;**92**(6):1328–32.
11. Karlsdottir SN, Halloran JW. Formation of oxide Films on zirconium diboride–silicon carbide composites during oxidation: relation of sub-

scale recession to liquid oxide flow. *J Am Ceram Soc* 2008;**91**(11): 3652–8.
12. Karlsdottir SN, Halloran JW, Grundy AN. Zirconium transport by liquid convection during oxidation of zirconium diboride–silicon carbide. *J Am Ceram Soc* 2008;**91**(1):272–7.
13. Karlsdottir SN, Halloran JW. Oxidation of ZrB_2–SiC: influence of SiC content on solid and liquid oxide phase formation. *J Am Ceram Soc* 2009;**92**:481–6.
14. Karlsdottir S, Halloran J, Bellosi A, Monteverde F. Oxidation of ZrB2–SiC: comparison of furnace heated coupons and self-heated ribbon specimens. In: *Proceedings of ICACC—31st international conference on advanced ceramics and composites*. 2007. p. 327–36.
15. Russ JC. *The image processing handbook*. second ed. Florida: CRC Press; 1995. p. 33–45.
16. Cubicciotti D. The melting point-composition diagram of zirconium–oxygen system. *J Am Chem Soc* 1951;**73**(5):2032–5.
17. CRC handbook of chemistry and physics, 89th ed., 2008–2009, Section 19 – emissivity of total radiation for various materials.
18. Fahrenholtz WG. Thermodynamic analysis of ZrB_2–SiC oxidaiton: formation of a SiC-depleted region. *J Am Ceram Soc* 2007;**90**:143–8.
19. Fahrenholtz WG. The ZrB_2 volatility diagram. *J Am Ceram Soc* 2005;**88**:3509–12.
20. Mieskowski DM, Mitchell TE, Heuer AH. Bubble formation in oxide scales on SiC. *J Am Ceram Soc* 1984;**67**. C-17–C-18.
21. Hirschfelder JO, Curtiss CF, Bird RB. *Molecular theory of gases and liquids*. New York: John Wiley & Sons Inc.; 1954. p. 165, 599.
22. Stull DR, Prophet H, NSRDS, JANAF Thermochemical Tables, National Bureau of Standards, NBS 27, second ed., Washington DC, 1971.